Load Transfer Mechanism of Geotextile-reinforced Sand Layer over Semi-rigid Column-improved Soft Soil

by

Pei-Chen WU[a]
Email: peichen.wu@connect.polyu.hk

Wen-Bo CHEN[b]
Email: geocwb@gmail.com

Wei-Qiang FENG[c]
Email: fengwq@sustech.edu.cn

Jian-Hua YIN[a]
Email: cejhyin@polyu.edu.hk

Tsz-On HO[c]
Email: tsz.on.ho@connect.polyu.hk / Ryan-TO.Ho@arup.com

and

Shu-Ran Huang[a]
Email: shu-ran.huang@polyu.edu.hk

[a]Department of Civil and Environmental Engineering
The Hong Kong Polytechnic University, Hong Kong, China

[b]College of Civil and Transportation Engineering
Shenzhen University, China

[c]Department of Ocean Science and Engineering,
Southern University of Science and Technology, Shenzhen, China

[d]Ove Arup & Partners Hong Kong Ltd (a former Postdoctoral Fellow in Department of Civil and Environmental Engineering, The Hong Kong Polytechnic University)

Abstract

Many design guidelines have been proposed for piled embankments, most of which consider piles or columns as rigid inclusions. In this study, a small-scale physical model test was performed to investigate the load transfer mechanism of a geotextile-reinforced (GR) sand layer over a soft subsoil improved by semi-rigid columns. A multi-stage load was applied at the top of the sand layer until the columns started to yield. When the columns yielded, a reverse load transfer was observed. Vertical stresses were measured and analyzed in terms of efficacy and stress reduction ratio (*SRR*) with a comparison of existing design guidelines for assessing soil arching. Among the reviewed guidelines, the approach recommended by the Dutch guidelines provided the closest results to the experimental data, whereas the one adopted by the American guidelines predicted well the change in efficacy and *SRR* under different surcharge loads. However, the load transfer mechanism after the yielding of columns is beyond the scope of the existing design guidelines. In addition, it was found through regression analysis that the increment of vertical stresses on columns and surrounding soil followed an inclined line under partially undrained conditions during loading stages and a curve during consolidation.

Keywords: Semi-rigid columns, Geotextile, Load transfer mechanism, Soft soil, Physical model test

1. Introduction

Recently, deep cement mixing (DCM) has been widely applied as a ground improvement technique in Hong Kong. In the third runway system project of Hong Kong International Airport, a layer of geosynthetic-reinforced (GR) load transfer platform (LTP) was designed over the soft soil treated using DCM columns before reclamation work [1, 46]. Similar to geosynthetic-reinforced column-supported (GRCS) embankments, the load transfer mechanism plays a significant role in reducing settlements, improving the bearing capacity of soft ground, and shortening the construction period.

The load transfer mechanism usually functions with the soil arching phenomenon in pile- or column-supported embankments with or without geosynthetic reinforcements [12, 27, 32, 38]. A family of friction models was established based on Terzaghi's soil arching theory [28, 30]. Then, the method of load-displacement compatibility (LDC) analysis was proposed by Filz et al. [9] to consider the relationship between settlement and soil arching in GRCS embankments. Another approach to investigate soil arching is to conduct three-dimensional physical model tests. These tests take into account factors such as the consolidation of subsoils and the potential membrane effect of geosynthetic reinforcements (GRs). In these tests, subsoils are either real soils [57] or simulated using other materials, such as foams [25, 30, 33, 34] and water bags [41,42]. In recent decades, full-scale and field tests have been conducted to explore the development of soil arching and the influence of cyclic loadings on the development of soil arching [41, 42, 58].

In the majority of experiments, piles are modeled by small concrete piles or rigid blocks. However, it is worth noting that the conclusions drawn from these experiments may not be

directly applicable to semi-rigid or flexible columns, such as columns made of cement-treated soft soil, stones, or sand. Significant lateral deformations of stone columns and sand piles can have a substantial impact on the load transfer mechanism and the development of soil arching, particularly when the surrounding soil cannot provide sufficient confining pressure. The lateral deformations of semi-rigid columns, such as DCM columns, are relatively smaller than those of stone columns and sand piles. Many studies have focused on the bearing capacity and consolidation behavior of DCM column-treated soft soil under embankment loadings [13, 26, 48, 53, 54]. Finite element methods were adopted to study the performance of GR embankments supported by DCM columns [23, 24, 40, 46, 50]. However, the structuration and bonding formed within the cement-treated soil may break under significant loading levels, which can lead to failure or strain softening behavior of cement-treated soils [17, 50]. Current design guidelines for GRCS embankments fail to capture the progressive failure and strain softening of DCM columns, which were reported and simulated by Yapage et al. [48, 49]. In addition, only a limited number of studies have focused on the load transfer mechanism in semi-rigid columns, geosynthetics, and soils.

In this study, a small-scale physical model test for a geotextile-reinforced (GR) sand layer over a soft subsoil improved using cement-treated soil columns was conducted to investigate the load transfer mechanism of semi-rigid column-supported embankments. A multi-stage surcharge load was applied until the columns yielded, which was identified by a sudden drop in vertical stress on the columns and a sudden increase in settlement.

2. Experiment setup and testing program

The physical model test was conducted in a steel tank with dimensions of 1000 mm (length) × 600 mm (width) × 800 mm (depth), as shown in Figure 1. Six cement-treated soil columns were installed in the subsoil of Hong Kong marine deposits (HKMD) overlaid by a GR sand layer. Similar setups were adopted by Zaeske [57] and van Eekelen et al. [33], in which the repeatability has been proved by dozens of tests. A multi-stage surcharge load was applied using a self-designed loading system equipped with a reaction frame and six pneumatic cylinders with a maximum output vertical stress of 200 kPa. The materials and transducers used in the model test are described in the following sections.

2.1 Materials

The subsoil in the physical model test was made through the reconstitution of the HKMD originally excavated from the coastal area of Lantau Island in Hong Kong [45]. HKMD is a type of dark grey soft soil with high compressibility and notable plasticity, whose basic properties are listed in Table 1. It should be noted that the effective cohesion of HKMD is nearly zero [7, 51]. The properties of the sand used in this study are listed in Table 1.

A piece of woven geotextile with a size of 1000 mm × 600 mm was prepared and framed with a pair of rectangular stainless-steel casing trims with an outer size of 950 mm × 550 mm and an inner size of 900 × 500 mm, as shown in Figure 2. Considering the focus of this study is on the vertical deformation and the load transfer mechanism of vertical stresses acting on the columns, geotextile, and surrounding soils, it is imperative to control the movement of the geotextile in the horizontal direction in order to eliminate any potential impact on the strain within the geotextile and the load distribution. The casing trims were used to restrict the

129 horizontal sliding/displacement of the geotextile but allow free vertical movement with the
130 settlement of the underlying soil during the loading tests.

131

132 The tensile properties of the woven geotextile were determined using the wide-width strip
133 method (ASTM D4595). The secant tensile modulus (J_s) of the geotextile is 680 kN/m in the
134 longitudinal direction and 150 kN/m in the transversal direction. The tensile strength of the
135 geotextile is 69 kN/m in the longitudinal direction and 17.3 kN/m in the transversal direction.
136 Geotextiles with similar tensile moduli were used in small-scale physical model tests conducted
137 by other researchers [25, 33, 34].

138

139 The semi-rigid columns adopted in this physical model were cement-treated soil columns with
140 a diameter of 100 mm and a length of 400 mm. To ensure consistency of quality, the cement-
141 treated soil columns with a cement content of 20% in terms of the dry mass of cement to the
142 dry mass of HKMD were prefabricated individually, in a similar manner to cast concrete
143 specimens. Reconstituted HKMD with an initial water content of 100% was thoroughly mixed
144 with ordinary Portland cement (OPC) by a concrete mixer for 10 min. Cement-soil mixtures
145 were subsequently cast into a PVC mold with an inner diameter of 100 mm by five layers.
146 Immediately after filling each layer, the PVC mold containing the cement-soil mixtures was
147 put on a vibration table and subjected to vibration for at least 60 s to avoid large voids in the
148 mixture. The cement-soil mixture transformed into solid columns after 24 h. After being
149 demoulded from the PVC mold and wrapped with plastic sheet, the columns were stored in a
150 chamber with a temperature of 20℃ and relative humidity of 90% for curing of 28 days. Similar
151 approaches of fabricating cement-treated soil columns were adopted by Yin and Fang [53] and
152 Ho et al. [13], owing to the advantage of producing columns of uniform quality for physical

153 model tests. The columns were installed in the physical model after 28 d of curing. Unconfined
154 compression (UC) tests with a strain rate of 1 mm/min were conducted on cement-treated
155 HKMD specimens with a diameter of 100 mm and a length of 200 mm after 28-day curing to
156 obtain an average UC strength q_u = 0.53 MPa and a secant Young's modulus E_{50} = 70 MPa.
157 E_{50} was determined by the stress at 50% of the UC strength to the axial strain corresponding to
158 this stress [14, 21].

159

160 *2.2 Transducers*

161 Earth pressure cells (EPCs) with capacities of 0.2 MPa and 2 MPa were used to measure the
162 vertical stresses at different locations. Two pore pressure transducers (PPTs) were placed at
163 different locations in the subsoil. Linear variable differential transformers (LVDTs) were used
164 to measure the settlements at the top surface of the sand layer. Load cells were used to record
165 the loading output of the loading system. An NI PXIe 4331 datalogger was used to record the
166 voltage signals from EPCs, PPTs, LVDTs, and load cells.

167

168 *2.3 Model preparation and setup*

169 Lubricant was applied to the side walls of the physical model tank to minimize the effect of the
170 side friction between the walls and soils. Intact HKMD was thoroughly mixed with additional
171 water to form a slurry with a water content of 100% and was subsequently carefully poured
172 into the tank to minimize the air trapped inside the soil. The consolidation of the slurry under
173 a uniform load of 5.35 kPa was then conducted. Prefabricated vertical drain bands (PVDs) were
174 employed to speed up the consolidation process. PVDs were removed after consolidation.
175 Metal pipes with an inner diameter of 100 mm were inserted vertically into the subsoil guided
176 by a wooden plate with circular holes. Level rulers were used to check the verticality of the

177 pipes. Soil inside the metal pipes was extracted along with these pipes forming holes in the
178 subsoil for the installation of prefabricated cement-treated soil columns. After carefully
179 inserting the columns into the holes, cement slurry with a cement content of 20% was poured
180 into the holes to fill the gap between the columns and the surrounding soil. It is worth
181 mentioning that the method of installing cement-treated soil columns used in this study is
182 different from the real practice of constructing DCM columns. The effect of in-situ mixing
183 procedures on the properties of the columns and surrounding soils is not considered in this
184 study. Eight EPCs were placed at the top of the HKMD subsoil improved by cement-treated
185 soil columns, as shown in Figure 1.

186

187 To simulate the load transfer platform used in the third runway system project of Hong Kong
188 International Airport, a sand blank with a thickness of 50 mm was placed on top of the subsoil
189 before installing the geotextile and the EPCs for measuring the vertical stress over the
190 geotextile. The total thickness of the sand layer reached 350 mm after filling another six layers
191 of sand (each with a thickness of 50 mm). The construction of the sand layer took
192 approximately 15 d. The total weight and volume of the sand were controlled to obtain a sand
193 fill with a relative density of 80%, and a rigid porous plate was placed on the top of the sand to
194 serve as a loading plate and a platform for setting the LVDTs.

195

196 *2.4 Geometrics and scale effects*

197 A certain height of embankments is required by the current design guidelines so that soil
198 arching can be fully developed. The GR sand layer in this study was 0.35 m, which was higher
199 than the minimum height recommended by BS 8006 [3], Dutch design guidelines [36], and the

Federal Highway Administration (FHWA) of the United States [29] under the geometrical configuration of the physical model test, namely 0.15, 0.22, and 0.33 m, respectively.

Without scaling, stress and time in this physical model test were the same as those in the geotechnical prototype, which requires other variables to be scaled down accordingly [4, 44], as shown in Table 2. The same approach was also adopted by van Eekelen et al. [33] to avoid considering stress-dependent behavior of filling materials. They also clarified that it is not necessary to apply scaling rules when comparing the measured results with the results calculated by analytical models. The scale of the physical model test was approximately 1:6 for the diameter and spacing of the columns in an embankment reported by Jamsawang et al. [16].

3. Experiment results

3.1 Settlement and excess pore pressure

A multi-stage loading test was started five days after the construction of the sand layer using the self-designed loading system following a loading sequence of 10, 20, 40, and 80 kPa. Surface settlements were measured during the loading tests. Each loading test was conducted until the excess pore pressure was nearly fully dissipated. Figure 3(a) shows the actual load applied at the top of the sand layer and the surface settlement, measured using load cells and LVDTs, respectively. The surface settlement was below 20 mm under the applied load of 10, 20, and 40 kPa, showing the effectiveness of cement-treated soil columns in controlling settlement. A significant increase in surface settlement was observed when the applied load reached 80 kPa. Figure 3(b) plots the final settlement under each load stage. The shape of the

223 settlement-log(load) curve is similar to typical *e*-log(σ) curves obtained from oedometer tests
224 covering both over-consolidated and normally consolidated states. The composite ground of
225 HKMD improved by cement-treated soil columns under the geotextile-reinforced sand fill
226 exhibited a low compressibility when the applied load was lower than 40 kPa; however, it
227 showed a high compressibility when the applied load reached 80 kPa. The significant
228 difference could be attributed to the yielding of the cement-treated soil columns, which is
229 discussed in the next section.

230

231 Figure 4 presents the excess pore pressures in the HKMD measured over time using PPT1 and
232 PPT2. When the applied load was smaller than 80 kPa, no significant difference in the
233 measured excess pore pressures was observed between the bottom level (PPT1) and middle
234 level (PPT2) of the HKMD. Rapid dissipation of excess pore pressure at both levels was
235 observed at the beginning of each loading stage. As the applied load approached 80 kPa, it was
236 observed that the excess pore pressure measured at the bottom of the HKMD was greater than
237 that measured at the middle level. In addition, the excess pore pressure at the middle level
238 dissipated faster than that at the bottom. The observed responses of the excess pore pressure
239 were probably attributed to the different drainage paths for the soils at different locations and
240 yielding of the columns that changed the stress state and drainage situations for the PPTs at
241 different locations. It should be noted that the yielded columns might have lateral expansion
242 towards the surrounding soil, resulting in an increase in lateral stress and pore water pressure
243 inside the surrounding soil [6, 54].

244

3.2 Vertical stress

Vertical stresses measured using EPCs at different locations are presented in Figure 5. Figures 5(a) and 5(b) show the vertical stresses above the GR. There was no significant difference observed between the vertical stress measured by EPC12 and that measured by EPC15. A notable difference between the vertical stress measured by EPC13 and that measured by EPC14 was observed after 80 d when the cement-treated soil columns yielded. Figures 5(c) and 5(d) present the vertical stresses (beneath the GR) at the top of the columns and the HKMD subsoil, respectively. Before the yielding of the columns, the vertical stress measured by EPCs on each column did not exhibit significant differences. However, when the columns started to yield, there was a nonnegligible difference in the vertical stresses among different columns. This difference could be attributed to the eccentric loading after the yielding of the columns and different boundary effects. It should also be noted that the vertical stresses presented here were based on local measurements. The limitations of the local measurements are discussed in Section 5. Figure 5(e) shows that the vertical stresses at the bottom of the HKMD subsoil were smaller than those at the top. This could be attributed to the skin friction between the columns and the surrounding soil. Comparing the excess pore pressure with the vertical total stress at the bottom of the HKMD subsoil, it can be observed that the excess pore pressure was higher than the vertical total stress at the beginning of the loading test. This could be attributed to additional lateral stress caused by the yielded columns and Mandel-Cryer effect [10] or creep effect of the HKMD [55].

To better address the mechanism of load transfer, the model test is divided into three zones: column, strip, and square zones, as shown in Figure 6(a). The column zone covers the cement-treated soil columns and the portion of the sand layer above the columns, the strip zone is the

area between two adjacent column zones, and the square zone is the area enclosed by four strip zones. Strip and square zones are similar to those adopted by van Eekelen et al. [36]. It should be noted that the difference between vertical stresses above and beneath the geotextile in the column zone may be significant, depending on the development of the membrane effect of the geotextile. The circular cross-section of columns can be converted into a square with an equivalent size of *a*. The area influenced by each column is illustrated using a column-soil unit, as shown in Figure 6(b).

Figure 7(a) shows the average vertical stress in the column zones. For the first two loadings, the vertical stresses above and beneath the geotextile show no discernible difference, indicating that the membrane effect of the geotextile was not fully mobilized. As the development of the membrane effect depends on the deflection of the geotextile related to the differential settlements between the columns and surrounding soft soil, it can be deduced that the differential settlements during the first two loading stages were not remarkable. When the load increased to 40 kPa, a significant difference was observed between the vertical stresses above and beneath the geotextile, indicating that a certain settlement occurred, which induced a noticeable tension that caused the development of the membrane effect in the geotextile. Owing to the membrane effect, the load taken by the geotextile was transferred to adjacent columns, thereby increasing the vertical stress beneath the geotextile in the column zones. When the applied load was increased to 80 kPa, the vertical stresses above and beneath the geotextile in the column zones reached their peak values, indicating the yielding of columns. The yielding of columns induced a dramatic settlement on the surface of the sand layer, as shown in Figure 3. After the test was completed, the column beneath EPC10 was retrieved from the physical model. This column had a typical shear failure, as shown in Figure 7(a). After the test was completed, the column beneath EPC10 was retrieved from the physical model. This column

had a typical shear failure, as shown in Figure 7(a). It is important to mention that the main focus of this study was on the load transfer before and after the yielding of cement-treated soil columns. The physical model test did not specifically delve into the failure modes of the soft ground improved by cement-treated soil columns, or the failure modes of each column installed in this test. Despite the yielding of the columns, the geotextile can continue to transfer the load to the columns. This load transfer could be due to the large differential settlements between the columns and surrounding soil as more loads could be transferred back to the surrounding soil. Considering the progressive failure of cement-treated soil columns, the membrane effect of the geotextile may accelerate the yielding of columns. In addition, the yielding stress of the columns in the physical model test was lower than the UC strength (0.53 MPa), which is uncommon as the strength of cement-treated soil columns under a confining pressure is normally higher than the unconfined compressive strength. Possible reasons could be: (1) the length-to-diameter ratio of the columns was 4:1, which was higher than that of the specimens for the UC tests (2:1), (2) the clamping effect inherent in UC tests, and (3) the local measurement of the vertical stress, which is discussed in Section 5.

Figure 7(b) shows the average vertical stresses above and beneath the geotextile in the strip and square zones, where the vertical stresses above the geotextile were greater than those beneath the geotextile. It is interesting to note that the vertical stress above the geotextile in the strip zone exceeded the applied load immediately after the load was applied. However, the increase in the vertical stress above the geotextile in the square zone did not exceed the applied surcharge load. At the beginning of each loading stage, the geotextile strips supported by two adjacent columns worked together with the columns, forming an “equivalent bridge” to participate in the transfer of load. In addition, given the partially undrained condition of the surrounding soil at that moment, the vertical stress above the geotextile in the strip zone was

compatible with that above the geotextile in the column zone before the yielding of columns. However, as the excess porewater pressure dissipated, the soil in between the columns started to settle. This soil settlement initiated a load transfer process, wherein the load was transferred from the square zone of the geotextile to the strip zone and subsequently to the columns, resulting in a decrease in the vertical stresses above the geotextile in both the square and strip zones. As mentioned earlier, the yielding of the columns resulted in a reverse load transfer from columns to the geotextile when the surcharge load increased to 80 kPa. Thus, the reverse load transfer significantly increased the load above the geotextile in the strip zone. However, the increase in vertical stress after the yielding of columns could also be attributed to the geometry change of the load distribution in the strip zones, which probably affected the local measurement of the vertical stress.

3.3 Load distribution

Load parts A, B, and C

According to van Eekelen [33, 34], the load transfer in embankments can be divided into load parts *A, B*, and *C*, which are the portions of the load acting on columns, transferred to GR, and supported by the subsoil, respectively, as illustrated in Figure 8. In this study, the vertical stresses above and beneath the geotextile in the column zone were used to calculate load parts *A* and *A* + *B*, respectively, whereas those beneath the geotextile in the strip and square zones were used to determine load part *C*. The equations for determining load parts A, B, and C are provided as follows.

$$A = \sigma_c^a A_c \tag{1}$$

$$B = \left(\sigma_c^b - \sigma_c^a\right) A_c \tag{2}$$

342 $$C = \sigma^{b}_{strip} A_{strip} + \sigma^{b}_{square} A_{squre} \quad (3)$$

343 where σ^{a}_{c} and σ^{b}_{c} are the vertical stresses above and beneath the geotextile in the column
344 zone, respectively, σ^{b}_{strip} represents the vertical stress beneath the geotextile in the strip zone,
345 σ^{b}_{square} is the vertical stress beneath the geotextile in the square zones, and A_c, A_{strip}, and A_{square}
346 are the areas of the column, strip , and square zones within each column-soil unit, respectively.
347 σ^{a}_{strip} and σ^{a}_{square} are the vertical stresses above the geotextile in the strip and square zones,
348 respectively. σ^{a}_{strip} and σ^{a}_{square} are not included in the above equations but are used in the
349 following discussion. σ^{a}_{c}, σ^{b}_{c}, σ^{b}_{strip}, σ^{b}_{square}, σ^{a}_{strip}, σ^{a}_{square}, A_c, A_{strip}, and A_{square} are
350 illustrated in Figure 6.

351

352 Figure 9 shows load parts *A*, *B*, and *C* (per column-soil unit) calculated using the vertical
353 stresses measured at different locations and time points. In the first loading stage, there was no
354 significant difference between load parts *A* and *C*, and load part B was nearly zero, indicating
355 a slight effect of the geotextile. As the surcharge load increased, load part *A* became the largest
356 portion among the three load parts. A significant reduction occurred in the load taken by the
357 HKMD subsoil. The increase in load part *B* indicated that the geotextile started to contribute
358 to the load redistribution. However, load part *A* decreased when the columns started to yield.
359 After the yielding of columns, load part *C* became the dominant portion.

360

361 The sum of load parts *A* + *B* + *C* and the total applied load per soil-column unit are shown in
362 Figure 9. When the applied load was 10 and 20 kPa, the sum of the load parts *A* + *B* + *C* agreed
363 well with the applied load per soil-column unit. When the load was 40 kPa, the sum of the load

parts $A + B + C$ was smaller than the applied load per soil-column unit. This was mainly due to the local measurement of the vertical stress using EPCs, which is discussed in Section 5. When the applied load reached 80 kPa, there was a significant difference between the sum of the load parts $A + B + C$ and the applied load per soil-column unit. This could be attributed to the yielding of the columns, which might change the area of the column zones.

Load transfer mechanism

To investigate the load transfer mechanism of the GR sand layer over the semi-rigid column-improved soft soil under surcharge loads, the vertical stresses in the column, strip, and square zones have been analyzed at different stages.

Figure 10(a) shows the relationships between the vertical stresses in the column and square zones (above the geotextile) in different stages. In each loading stage, the vertical stresses in both the column and square zones increased until the subsoil started to consolidate. The ratio of the increment of σ_c^a to the increment of σ_{square}^a was nearly identical in each loading stage. Linear regressions were conducted on σ_c^a and σ_{square}^a in the loading stages, as indicated by the dotted lines in Figure 10(a). The slope is similar to the stress concentration ratio, which is an important index representing the load distribution on the soft soil improved by columns [12,52]. The average slope of the dotted lines in the four loading stages is 2.44. As the surcharge increased in a short period of time, the subsoil was considered to be in a partially undrained condition during the loading stages. A linear envelope line with a slope of 6.16 can be drawn by fitting the relationship between σ_c^a and σ_{square}^a before consolidation at each loading stage (immediately after load application). Soil arching in the overlaid GR sand layer started to

387 develop when the consolidation settlement of the subsoil increased, causing an unloading
388 process to occur in the square zone. When the consolidation was completed, the load transfer
389 paused, resulting in a stable state, which can be enveloped by a line with a slope of 13.73. In
390 this physical model test, the slope of the envelope line after the consolidation of the subsoil
391 was approximately doubled compared to that before consolidation. The two envelop lines
392 before and after the consolidation of the subsoil formed a region where the vertical stress
393 increments caused by the different surcharge loads followed a path of an inclined line under
394 the partially undrained condition during loading stages and a curve during consolidation.
395 However, the path crossed the lower boundary of the region (the envelope line describing the
396 state immediately after the application of load) as the columns started to yield.

397

398 Figure 10(b) shows the relationships between the vertical stresses in the column and strip zones
399 (above the geotextile) at different stages. Linear functions can be used to fit the relationship
400 between σ_c^a and σ_{strip}^a during the loading stages, as shown by the dotted lines in Figure 10(b).
401 The dotted lines are nearly parallel with an average slope of 0.66, indicating that the vertical
402 stress increment in the strip zone was larger than that in the column zone owing to the partially
403 undrained condition during the loading stages. Two envelope lines with slopes of 1.85 and
404 11.76 representing the stages before and after the consolidation, respectively, are plotted. The
405 slope of the envelope line after consolidation is approximately six times greater than that before
406 consolidation, indicating that the consolidation of the subsoil largely affected the load transfer
407 between the column and strip zones above the geotextile. An inclined line under the partially
408 undrained condition during loading stages followed by a curve during consolidation was also
409 observed in the region formed by the two envelope lines before and after consolidation. After
410 the columns yielded, the path shifted outside of the defined region.

411

412 Figure 10(c) shows the relationships between the vertical stresses in the column and square
413 zones (beneath the geotextile) at different stages. Similarly, linear functions can be used to fit
414 the relationship between σ_c^b and σ_{square}^b during the loading stages, as indicated by the dotted
415 lines in Figure 10(c). These dotted lines are nearly parallel, and have an average slope of 7.21,
416 which represents the stress concentration ratio of the vertical stress in the column zone to that
417 in the square zone. The value agrees with the typical stress concentration ratio of GRCS
418 embankments with semi-rigid columns, which ranges from 5 to 10 [12]. Two envelope lines
419 with slopes of 20.23 and 47.25 representing the stages before and after the consolidation,
420 respectively, are plotted. The ratio between the slopes of the envelop lines before and after
421 consolidation is approximately 2, which is similar to the ratio obtained from Figure 10(a). In
422 addition, a similar path of an inclined line under the partially undrained condition during the
423 loading stages followed by a curve during consolidation can be also observed. The relationship
424 between the vertical stresses in the column and square zones after the yielding of the columns
425 is similar to that in the loading stages before yielding.

426

427 The relationships between the vertical stresses in the column and strip zones beneath the
428 geotextile at different stages are fitted by dotted lines with an average slope of 5.07, as shown
429 in Figure 10(d). Two envelope lines with slopes of 11.41 and 22.67, representing the stages
430 before and after the consolidation, respectively, are plotted. The slope of the envelope line after
431 consolidation is approximately 1.7 times greater than that before consolidation. A similar path
432 of an inclined line under the partially undrained condition in the loading stages followed by a
433 curve during consolidation can be also observed. The relationship between the vertical stresses

434 in the column and square zones after the yielding of the columns is similar to those in the
435 loading stages before yielding.

436

437 **4 Assessment of arching effect**

438 Many scholars have started to consider the strain-softening and progressive failure of column-
439 supported embankments [49, 56, 59]. However, only the elastic behavior of columns/piles is
440 considered in the current design methods for determining arching effect. Therefore, it is worth
441 investigating the load transfer mechanism after the yielding of the columns with the comparison
442 to the results provided by the current design methods in order to improve the design methods
443 not only for guiding the design but also for analyzing and explaining the reasons behind failures
444 and geohazards.

445

446 *4.1 Assessment of arching effect using current design methods*

447 According to Hewlett and Randolph method, pile (or column) efficacy *E* is the proportion of
448 the load taken by columns. In this study, the efficacy of the cement-treated soil columns is
449 calculated as follows:

450 $$E_A = \frac{A}{(\gamma H + p)s^2} \tag{4}$$

451 $$E_{A+B} = \frac{A+B}{(\gamma H + p)s^2} \tag{5}$$

452 where E_A is the efficacy in which the effect of geotextile is ignored, E_{A+B} is the efficacy in
453 which the effect of geotextile is considered, *A* and *B* represent load parts *A* and *B* determined
454 by Eqs. (1) and (2), respectively, *p* is the surcharge load at the top of the GR sand layer, *s* is

455 the size of the column-soil unit influenced by the column, γ is the unit weight of the
456 embankment fill, and H is the height of the embankment.

457

458 *SRR* is an index used to assess the development of arching. $SRR = 1$ indicates that no arching
459 effect occurs in the filling materials. A smaller *SRR* value indicates a more significant arching
460 effect. In this study, *SRR* can be calculated as:

461 $$SRR = \frac{C}{(\gamma H + p)(s^2 - a^2)} \tag{6}$$

462 where *C* indicates load part *C* determined by Eq. (3).

463

464 Additionally, four commonly used methods from the current design guidelines for GRCS
465 embankments are adopted to predict the efficacy *E* and stress reduction ratio *SRR*.

466

467 *Hewlett and Randolph's method*

468 A semi-spherical arching model was proposed to analyze the load transfer in GRCS
469 embankments and adopted in the French guidelines and BS 8006 as an additional method. The
470 critical location is assumed to be at the crown of semicircular arches or pile caps. Eqs. (4)–(9)
471 are the equations for determining the efficacy and stress reduction ratio.

472 Critical location at the crown of arches:

473 $$E_{crown} = 1 - \left[1 - \left(\frac{a}{s}\right)^2\right](\alpha_1 - \alpha_1\alpha_2 + \alpha_3) \tag{7}$$

474 $$SRR_{crown} = \alpha_1 - \alpha_1\alpha_2 + \alpha_3 \tag{8}$$

475 $$\alpha_1 = \left[1-\left(\frac{a}{s}\right)\right]^{2\left(K_p-1\right)},\ \alpha_2 = \frac{s}{\sqrt{2}H}\left(\frac{2K_p-2}{2K_p-3}\right), \text{ and } \alpha_3 = \frac{s-a}{\sqrt{2}H}\left(\frac{2K_p-2}{2K_p-3}\right) \quad (9)$$

476 Critical location at pile caps:

477 $$E_{cap} = \frac{\beta}{1+\beta} \quad (10)$$

478 $$SRR_{cap} = \frac{1}{\left(1+\beta\right)\left[1-\left(a/s\right)^2\right]} \quad (11)$$

479 $$\beta = \frac{2K_p}{(K_p+1)(1+a/s)}\left[(1-a/s)^{-K_p} - (1+K_p a/s)\right] \quad (12)$$

480 where $K_p = \frac{1+\sin(\varphi')}{1-\sin(\varphi')}$, s is the column spacing, γ is the unit weight of the embankment fill,

481 H is the height of the embankment, a is the equivalent size of the column, and φ' is the

482 friction angle of the embankment fill. The surcharge load is converted into an additional height

483 $\Delta H = p/\gamma$ [41]. The efficacy and stress reduction ratio used for comparison are

484 $\min\left(E_{crown}, E_{cap}\right)$ and $\max\left(SRR_{crown}, SRR_{cap}\right)$, respectively.

485

486 *German EBGEO method*

487 German EBGEO [5] adopted the multi-shell arches theory of Zaeske [57]. In EBGEO, subsoil

488 support is considered only when calculating the tensile strain of GR. The efficacy and *SRR* are

489 calculated as follows:

490 $$E = \frac{(\gamma H + p - \sigma_{z0})s^2 + \sigma_{z0}a^2}{(\gamma H + p)s^2} \quad (13)$$

491 $$SRR = \frac{\sigma_{z0}}{(\gamma H + p)} \quad (14)$$

492 $$\sigma_{z0} = \lambda_1^{\chi}(\gamma + p/H)\left\{H(\lambda_1 + h_g^2\lambda_2)^{-\chi} + h_g\left[(\lambda_1 + h_g^2\lambda_2/4)^{-\chi} - (\lambda_1 + h_g^2\lambda_2)^{-\chi}\right]\right\} \quad (15)$$

493 where $h_g = s_d/2$ for $H \geq s_d/2$, and $h_g = H$ for $H < s_d/2$, $\chi = \frac{a(K_{crit}-1)}{\lambda_2 s_d}$,

494 $K_{crit} = \tan^2(45° + \frac{\varphi'}{2})$, $\lambda_1 = \frac{(s_d - a)^2}{8}$, $\lambda_2 = \frac{s_d^2 + 2as_d - a^2}{2s_d^2}$, s_d is the center-to-center spacing

495 between two diagonal columns, and p is the surcharge load.

496

497 *Adapted Terzaghi method*

498 Sloan et al. [31] extended Terzaghi's soil arching theory and proposed an adapted Terzaghi
499 method, which has been adopted in FHWA design guidelines [29]. The pile efficacy
500 determined by the adapted Terzaghi method can be expressed as follows:

501 $$E = 1 - SRR\left(1 - \frac{a^2}{s^2}\right) \quad (16)$$

502 $$SRR = \frac{\frac{\gamma}{\alpha}\left(1 - e^{-\alpha H}\right) + pe^{-\alpha H}}{(\gamma H + p)} \quad (17)$$

503 where $\alpha = p_c K_T \tan\varphi' / \left(s^2 - a^2\right)$ and p_c is the column perimeter. $K_T = 0.75$ is suggested
504 by Filz and Smith [8].

505

506 *Concentric Arches (CA) model*

507 The CA model is a three-dimensional (3D) soil-arching model adopted in the Dutch design
508 guidelines [36]. In the CA model, 3D concentric hemispherical arches are developed in square
509 zones, whereas two-dimensional (2D) concentric semicircle arches are developed in strip zones.
510 The pile efficacy is expressed as follows:

$$E = \frac{(\gamma H + p)s^2 - F_{GRsquare} - F_{GRstrip}}{(\gamma H + p)s^2} \quad (18)$$

and the stress reduction ratio is:

$$SRR = \frac{F_{GRstrip} + F_{GRsquare}}{(\gamma H + p)(s^2 - a^2)} \quad (19)$$

where $F_{GRsquare}$ and $F_{GRstrip}$ are the loads acting on the square and strip zones, respectively. van Eekelen et al. [35] presented in detail a method for determining $F_{GRsquare}$ and $F_{GRstrip}$.

4.2 Pile efficacy

Figure 11(a) shows the changes in efficacy with surcharge load. When the surcharge was smaller than 40 kPa, the GR did not substantially increase the efficacy of the columns. As the surcharge increased, a significant difference between the efficacies with and without considering the membrane effect of the GR can be observed, indicating that the GR started to function. It was found that both the efficacies with and without considering the effect of the GR show a decrease during the process of increasing the surcharge load. This was due to the partially undrained condition of the subsoil, which delayed the load transfer. The differential settlements between the columns and surrounding soil increased with the consolidation of the subsoil, resulting in an increase in the deflection of the GR, and thus increasing the efficacy. The efficacy of the columns at the end of the consolidation slightly increased with an increase in surcharge load. This finding agreed with the results of a finite simulation conducted by van der Peet and van Eekelen [39]. A further increase in the surcharge load resulted in the yielding of the cement-treated soil columns.

Linear correlation relationships can be found between the efficacies with and without considering the membrane effect of the GR under different surcharge loads, as shown in Figure 12. The ratios of the efficacies with and without considering the effect of GR are 1.16, 1.09, 1.19, and 1.28, under the surcharge loads of 10, 20, 40, and 80 kPa, respectively. The values generally agree with the range (1.15 to 1.3) reported by Low et al. [25] obtained from a series of 2D physical model tests. The development of the membrane effect of GR is related to its deflection and the differential settlement between the columns and surrounding soil. However, no direct measurement has been carried out on the deflection of GR, which is one of the limitations of this physical model test, as discussed in Section 5.

Among the four design guidelines, the result of the adapted Terzaghi method agreed well with the trend of the efficacy calculated using the measured data considering the GR effect (after consolidation) before the yielding of the cement-treated soil columns. However, it should be noted that the results calculated by the adapted Terzaghi method are highly dependent on the value of K_T. Higher K_T values result in higher efficacies. Therefore, this method must be used with caution. Despite its failure to capture the changing trend of efficacy considering the GR effect, the CA model gave results similar to those calculated using the measured data. The results of the German EBGEO [5] method agreed well with the efficacy calculated using the measured data disregarding the effect of the geotextile.

4.3 SRR

Figure 11(b) shows the *SRR* calculated using the measured data and the current design methods. The *SRR* calculated using the measured data tended to decrease with increasing surcharge load, indicating that more significant arching occurred under a larger surcharge load. However, the

556 *SRR* increased during the loading stages, which could be explained by the partially undrained
557 condition within the short period of the loading stages. As the subsoil consolidated, the
558 differential settlements between the columns and surrounding soil increased, resulting in an
559 increase in the deflection of the geotextile, and thus reducing the *SRR*.

560

561 The adapted Terzaghi method captured the general decreasing trend of the *SRR* calculated using
562 measured data. When the surcharge load was small (below 40 kPa in this study), both the CA
563 model and Hewlett and Randolph's method provided *SRR* values similar to those calculated
564 using the measured data. However, the German EBGEO method gave an overestimated *SRR*
565 compared with the other methods. van Eekelen et al. [4] reported similar results and explained
566 that the German EBGEO method does not take into account the increase in arching caused by
567 consolidation.

568

569 *4.4 Discussion*

570 Hewlett and Randolph's method provided overestimated values in terms of the efficacy of
571 semi-rigid columns. However, the vertical stress acting on the columns calculated by Hewlett
572 and Randolph's method was generally smaller than those calculated by the German EBGEO
573 [5] method and the CA model [39]. Thus, this method should provide lower efficacies. Under
574 no surcharge load, Hewlett and Randolph's method resulted in an efficacy of 0.48, which was
575 smaller than the efficacy calculated using the CA model. The overestimated results of Hewlett
576 and Randolph's method were due to the height of the sand layer used in the calculation, which
577 was increased by the additional height converted from the surcharge loads. Therefore, Hewlett
578 and Randolph's method might not be suitable for embankments supported by semi-rigid
579 columns subjected to large surcharge loads.

The efficacies and *SRR*s calculated by the CA model, German EBGEO method, and Hewlett and Randolph method remained constant under the different surcharge loads. This was because these methods are based on limit state equilibrium, which can only determine a constant arching stress value. The amount of deformation required to achieve the arching state assumed by these methods remains unclear [19]. The actual deformations that occur in GRCS embankments are incompatible with the required deformations, which leads to different results for various arching models. In addition, the decrease in efficacy and the increase in *SRR* due to the yielding of columns are beyond the scope of the current design guidelines.

In addition, it should be pointed out that the consistency or contradiction between the testing results and prediction by the design guidelines in this study should not be simply applied to other cases without performing additional investigations to take into account scale and boundary effects. However, the comparisons presented here may serve as a valuable reference for future endeavors, such as conducting full-scale experiments and numerical analysis on the load transfer mechanism of geotextile-reinforced sand layer over soft soil improved by semi-rigid columns.

5. Limitations of the physical model test

For small-scale physical model tests, one inevitable limitation is the scale effect. However, conducting small-scale tests is an economical way to address specific engineering issues and provide references for numerical modeling that bridges small-scale tests to real projects. Further experimental and numerical studies should be conducted to investigate the influence of

603 different factors, such as column configurations, material properties, and loading conditions on
604 the load transfer mechanism. Two technical limitations are addressed in detail, as follows.

605

606 *5.1 Local measurement of vertical stress*

607 The distribution of vertical stress at the top of columns/piles is usually non-uniform. The
608 vertical stress tends to be greater near the periphery of columns/piles [11]. As the size of the
609 EPCs used in this study was smaller than the diameter of the cement-treated soil columns, the
610 measured vertical stress only represented the local vertical stress at the center of each column
611 instead of the overall average stress over each column. Therefore, the local measurement using
612 small-sized EPCs probably underestimated the load taken by the cement-treated soil columns,
613 indicating that the actual efficacies of the columns could be higher than those calculated using
614 measured vertical stresses.

615

616 *5.2 Deflection of GR*

617 The development of soil arching in GRCS embankments is related to the deflection of the GR
618 or the differential settlement between the columns and surrounding soil [15, 18]. Therefore, it
619 is important to measure the deflection of GRs. However, no direct measurement was performed
620 on the deflection of the GR in this small-scale physical model test. In full-scale experiments or
621 field tests, settlement plates can be installed above the GR or in the subsoil to monitor the
622 deflection of the GR or settlement of the subsoil. However, settlement plates were not
623 applicable in this study with the current setup. Nevertheless, the maximum sag of the GR in
624 the square zones can be estimated by the following equation proposed by King et al. [20]:

625 $$\delta_{s,\max} = 0.558\sqrt[3]{\frac{\sigma_{square}^{a}(s-a)^4}{J}} \quad (20)$$

where $\delta_{s,\max}$ is the maximum sag of the GR in the square zones. The calculated maximum sags under the surcharge loads of 10, 20, 40, and 80 kPa are 2.79, 5.13, 7.87, and 18.08 mm, respectively. Comparing the maximum sags with the ratios of efficacies with and without considering the effect of GR, it can be roughly revealed that the membrane effect of the GR on efficacy increases with the deflection of the GR.

Although the tensile modulus of geotextiles/geogrids was reported to have little effect on the efficacy of columns [22, 33, 34], it could affect the soil arching by influencing the deflection of GR, as indicated by Eq. (20). Considering that the current design methods reviewed in Section 4 follow the two-step design approach which assumes that arching actions are independent of the subsoil deformation and deflection of GR, the analysis on the load transfer mechanism in this study does not consider the influence of the tensile modulus of GR.

6. Findings and Conclusions

A small-scale physical model test was conducted to investigate the load transfer mechanism of a GR sand layer over a soft subsoil improved by semi-rigid columns. A multi-stage surcharge load was applied to the sand layer until the yielding of columns was observed. The arching effect was assessed and compared with the current design methods for GRCS embankments. The main findings and conclusions are as follows:

(a) Significant surface settlement was observed when the columns started to yield. The geotextile facilitated the load transfer between the columns and the subsoil.

(b) When the columns yielded, the reverse load transfer from the column zone to the strip zone was significant.

649 (c) Vertical stresses before and after the consolidation of the subsoil were enveloped with two
650 lines, creating a region where the increments of the vertical stresses followed an inclined
651 line under the partially undrained condition during loading stages, and a curve during
652 consolidation.
653 (d) Among the current design guidelines reviewed, the CA model of the Dutch guidelines
654 provided efficacy and *SRR* that were closest to those obtained from the local measurement
655 of vertical stress. The adapted Terzaghi method can predict well the change in efficacy and
656 *SRR* under different surcharge loads. However, the decrease in efficacy and the increase
657 in *SRR* due to the yielding of the columns are beyond the scope of the current design
658 guidelines.

659

Acknowledgments

The work in this paper is supported by a Research Impact Fund (RIF) project (R5037-18) and three General Research Fund (GRF) projects (PolyU 15210020; PolyU 15210322; PolyU 15226722) from Research Grants Council (RGC) of Hong Kong Special Administrative Region Government of China. The authors also acknowledge the financial support from Research Institute for Land and Space of The Hong Kong Polytechnic University and three grants (CD82, CD7A) from The Hong Kong Polytechnic University.

References

1. Airport Authority Hong Kong (2012) Expansion of Hong Kong international airport into a three-runway system project profile. http://www.epd.gov.hk/eia/register/profile/latest/esb250/esb250.pdf.
2. ASTM (2005) 4595 Standard Test Method for Tensile Properties of Geotextiles by the Wide-Width Strip Method. ASTM Standards.
3. BS 8006 (2010) Code of Practice for Strengthened/Reinforced Soils and Other Fills. British Standard Institution, UK
4. Butterfield R (1999) Dimensional analysis for geotechnical engineers. Geotechnique 49(3): 357-366. https://doi.org/10.1680/geot.1999.49.3.357
5. EBGEO (2010) Empfehlungen für den Entwurf und die Berechnung von Erdkörpern mit Bewehrungen aus Geokunststoffen e EBGEO, vol. 2 German Geotechnical Society, Auflage978-3-433-02950-3 (in German). Also available in English: Recommendations for Design and Analysis of Earth Structures using Geosynthetic Reinforcements e EBGEO, 2011. ISBN: 978-3-433-02983-1 and digital in English ISBN: 978-3-433-60093-1.
6. Fang Z, Yin JH (2007) Responses of excess pore water pressure in soft marine clay around a soil–cement column. International Journal of Geomechanics 7(3):167-175. https://ascelibrary.org/doi/10.1061/%28ASCE%2915323641%282007%297%3A3%28167%29
7. Feng WQ, Yin JH, Chen WB, Tan DY, Wu PC (2020) A new simplified method for calculating consolidation settlement of multi-layer soft soils with creep under multi-stage ramp loading. Engineering Geology 264:105322. https://doi.org/10.1016/j.enggeo.2019.105322

692 8. Filz GM, Smith ME (2006) Design of bridging layers in geosynthetic-reinforced, column-
693 supported embankments. Virginia Center for Transportation Innovation and Research.
694 http://hdl.handle.net/10919/46681
695 9. Filz GM, Sloan JA, McGuire MP, Smith M, Collin J (2019) Settlement and vertical load
696 transfer in column-supported embankments. Journal of Geotechnical and
697 Geoenvironmental Engineering 145(10):04019083.
698 https://ascelibrary.org/doi/10.1061/%28ASCE%29GT.1943-5606.0002130
699 10. Gibson RE, Gobert A, Schiffman RL (1989) On Cryer's problem with large displacements.
700 International Journal for Numerical and Analytical Methods in Geomechanics 13(3):251-
701 262. https://doi.org/10.1002/nag.1610130303
702 11. Han J, Gabr MA (2002). Numerical analysis of geosynthetic-reinforced and pile-supported
703 earth platforms over soft soil. Journal of geotechnical and geoenvironmental engineering
704 128(1):44-53. https://ascelibrary.org/doi/abs/10.1061/(ASCE)1090-0241(2002)128:1(44)
705 12. Han J, Wayne MH (2000) Pile-soil-geosynthetic interactions in geosynthetic reinforced
706 platform/piled embankments over soft soil. In Presentation at 79th annual transportation
707 research board meeting, Washington, DC.
708 13. Ho TO, Tsang DC, Chen WB, Yin JH (2020) Evaluating the environmental impact of
709 contaminated sediment column stabilized by deep cement mixing. Chemosphere
710 261:127755. https://doi.org/10.1016/j.chemosphere.2020.127755
711 14. Ho TO, Chen WB, Yin JH, Wu PC, Tsang DC (2021) Stress-Strain behaviour of Cement-
712 Stabilized Hong Kong marine deposits. Construction and Building Materials 274: 122103.
713 https://doi.org/10.1016/j.conbuildmat.2020.122103
714 15. Iglesia GR, Einstein HH, Whitman RV (2014) Investigation of soil arching with centrifuge
715 tests. Journal of Geotechnical and Geoenvironmental engineering 140(2): 04013005.
716 https://ascelibrary.org/doi/10.1061/%28ASCE%29GT.1943-5606.0000998

16. Jamsawang P, Yoobanpot N, Thanasisathit N, Voottipruex P, Jongpradist P (2016) Three-dimensional numerical analysis of a DCM column-supported highway embankment. Computers and Geotechnics 72:42-56. https://doi.org/10.1016/j.compgeo.2015.11.006
17. Kamruzzaman AH, Chew SH, Lee FH (2009) Structuration and destructuration behavior of cement-treated Singapore marine clay. Journal of geotechnical and geoenvironmental engineering 135(4):573-589. https://ascelibrary.org/doi/abs/10.1061/(ASCE)1090-0241(2009)135:4(573)
18. King DJ, Bouazza A, Gniel JR, Rowe RK, Bui HH (2017a) Load-transfer platform behaviour in embankments supported on semi-rigid columns: implications of the ground reaction curve. Canadian Geotechnical Journal 54(8):1158-1175. https://doi.org/10.1139/cgj-2016-0406
19. King DJ, Bouazza A, Gniel JR, Rowe RK, Bui HH (2017b) Serviceability design for geosynthetic reinforced column supported embankments. Geotextiles and Geomembranes 45(4):261-279. https://doi.org/10.1016/j.geotexmem.2017.02.006
20. King L, King D, Bouazza A, Gniel J, Rowe RK (2021) Design of geosynthetic reinforced column supported embankments using an interaction diagram. Geotextiles and Geomembranes 49(1):159-165. https://doi.org/10.1016/j.geotexmem.2020.09.010
21. Kitazume M, Terashi M (2013) The deep mixing method. CRC press, London
22. Lee T, van Eekelen SJM, Jung YH (2020) Numerical verification of the Concentric Arches model for geosynthetic-reinforced pile-supported embankments: applicability and limitations. Canadian Geotechnical Journal 58(3):441-454. https://doi-org.ezproxy.lb.polyu.edu.hk/10.1139/cgj-2019-0625
23. Liu KW, Rowe RK (2015) Numerical study of the effects of geosynthetic reinforcement viscosity on behaviour of embankments supported by deep-mixing-method columns.

741 Geotextiles and Geomembranes 43(6):567-578.
742 https://doi.org/10.1016/j.geotexmem.2015.04.020
743 24. Liu K W, Rowe RK, Su Q, Liu B, Yang Z (2017) Long-term reinforcement strains for
744 column supported embankments with viscous reinforcement by FEM. Geotextiles and
745 Geomembranes 45(4):307-319. https://doi.org/10.1016/j.geotexmem.2017.04.003
746 25. Low BK, Tang SK, Choa V (1994) Arching in piled embankments. Journal of
747 Geotechnical Engineering 120(11):1917-1938.
748 https://ascelibrary.org/doi/abs/10.1061/(ASCE)0733-9410(1994)120:11(1917)
749 26. Phutthananon C, Jongpradist P, Jongpradist P, Dias D, Baroth J (2020) Parametric analysis
750 and optimization of T-shaped and conventional deep cement mixing column-supported
751 embankments. Computers and Geotechnics 122:103555.
752 https://doi.org/10.1016/j.compgeo.2020.103555
753 27. Rui R, Zhai YX, Han J, Van Eekelen SJM, Chen C (2020) Deformations in trapdoor tests
754 and piled embankments. Geosynthetics International 27(2):219-235.
755 https://doi.org/10.1680/jgein.19.00014
756 28. Russell D, Pierpoint N (1997) An assessment of design methods for piled embankments.
757 Ground Engineering 30(10).
758 29. Schaefer VR, Berg RR, Collin JG, Christopher BR, DiMaggio JA, Filz GM, Bruce DA,
759 Ayala D (2017) Ground modification methods reference manual—Volume I and II.
760 Washington, DC: Federal Highway Administration.
761 https://www.fhwa.dot.gov/engineering/geotech/pubs/nhi16027.pdf
762 https://www.fhwa.dot.gov/engineering/geotech/pubs/nhi16028.pdf
763 30. Sloan JA (2011) Column-supported embankments: full-scale tests and design
764 recommendations. Doctoral dissertation, Virginia Tech

765 31. Sloan J, Filz GM, Collin J (2011) A generalized formulation of the adapted terzaghi
766 method of arching in column-supported embankments. In: Geo-Frontiers 2011: Advances
767 in Geotechnical Engineering, pp 798-805
768 https://ascelibrary.org/doi/abs/10.1061/41165(397)82
769 32. Terzaghi K (1943) Stress Conditions for Failure in Soils. In: Theoretical soil mechanics.
770 John Wiley & sons, Inc., New York, pp 11-15
771 https://doi.org/10.1002/9780470172766.fmatter
772 33. van Eekelen SJM, Bezuijen A, Lodder HJ, van Tol EA (2012a) Model experiments on
773 piled embankments. Part I. Geotextiles and Geomembranes 32:69-81.
774 https://doi.org/10.1016/j.geotexmem.2011.11.002
775 34. van Eekelen SJM, Bezuijen A, Lodder HJ, van Tol EA (2012b) Model experiments on
776 piled embankments. Part II. Geotextiles and Geomembranes 32:82-94.
777 https://doi.org/10.1016/j.geotexmem.2011.11.003
778 35. van Eekelen SJM, Bezuijen A, Van Tol AF (2013) An analytical model for arching in piled
779 embankments. Geotextiles and Geomembranes 39:78-102.
780 https://doi.org/10.1016/j.geotexmem.2013.07.005
781 36. van Eekelen SJM, Bezuijen A, Van Tol AF (2015) Validation of analytical models for the
782 design of basal reinforced piled embankments. Geotextiles and Geomembranes 43(1):56-
783 81. https://doi.org/10.1016/j.geotexmem.2014.10.002
784 37. van Eekelen SJ, Brugman MH (2016) Design guideline basal reinforced piled
785 embankments. CRC press.
786 38. van Eekelen SJ, Han J (2020) Geosynthetic-reinforced pile-supported embankments: state
787 of the art. Geosynthetics International 27(2):112-141.
788 https://doi.org/10.1680/jgein.20.00005
789

790 39. van der Peet TC, van Eekelen SJM (2014) 3D numerical analysis of basal reinforced piled
791 embankments. In: Tenth International Conference on Geosynthetics, pp 21-25
792 40. Waichita S, Jongpradist P, Schweiger HF (2020) Numerical and experimental
793 investigation of failure of a DCM-wall considering softening behaviour. Computers and
794 Geotechnics 119:103380. https://doi.org/10.1016/j.compgeo.2019.103380
795 41. Wang HL, Chen RP, Liu QW, Kang X (2019a) Investigation on geogrid reinforcement and
796 pile efficacy in geosynthetic-reinforced pile-supported track-bed. Geotextiles and
797 Geomembranes 47(6):755-766. https://doi.org/10.1016/j.geotexmem.2019.103489
798 42. Wang HL, Chen RP, Cheng W, Qi S, Cui YJ (2019b) Full-scale model study on variations
799 of soil stress in geosynthetic-reinforced pile-supported track bed with water level change
800 and cyclic loading. Canadian Geotechnical Journal 56(1):60-68.
801 https://doi.org/10.1139/cgj-2017-0689
802 43. Wijerathna M, Liyanapathirana DS, Jian Leo C (2017) Analytical solution for the
803 consolidation behavior of deep cement mixed column–improved ground. International
804 Journal of Geomechanics 17(9):04017065.
805 https://ascelibrary.org/doi/10.1061/%28ASCE%29GM.1943-5622.0000954
806 44. Wood DM (2003) Geotechnical modelling. Vol. 1. CRC press.
807 45. Wu PC, Yin JH, Feng WQ, Chen WB (2019) Experimental study on geosynthetic-
808 reinforced sand fill over marine clay with or without deep cement mixed soil columns
809 under different loadings. Underground space 4(4):340-347.
810 https://doi.org/10.1016/j.undsp.2019.03.001
811 46. Wu PC, Feng WQ, Yin JH (2020) Numerical study of creep effects on settlements and
812 load transfer mechanisms of soft soil improved by deep cement mixed soil columns under
813 embankment load. Geotextiles and Geomembranes 48(3):331-348.
814 https://doi.org/10.1016/j.geotexmem.2019.12.005

47. Yapage NNS, Liyanapathirana DS (2014) A parametric study of geosynthetic-reinforced column-supported embankments. Geosynthetics International 21(3):213-232. https://doi.org/10.1680/gein.14.00010

48. Yapage NNS, Liyanapathirana DS, Kelly RB, Poulos HG, Leo CJ (2014) Numerical modeling of an embankment over soft ground improved with deep cement mixed columns: case history. Journal of Geotechnical and Geoenvironmental Engineering 140(11):04014062. https://ascelibrary.org/doi/abs/10.1061/(ASCE)GT.1943-5606.0001165

49. Yapage NNS, Liyanapathirana DS, Poulos HG, Kelly RB, Leo CJ (2015) Numerical modeling of geotextile-reinforced embankments over deep cement mixed columns incorporating strain-softening behavior of columns. International Journal of Geomechanics 15(2):04014047. https://ascelibrary.org/doi/abs/10.1061/(ASCE)GM.1943-5622.0000341

50. Yapage NNS, Liyanapathirana DS (2019) A review of constitutive models for cement-treated clay. International Journal of Geotechnical Engineering 13(6):525-537. https://doi.org/10.1080/19386362.2017.1370878

51. Yin JH (2001) Stress-strain-strength characteristics of soft Hong Kong marine deposits without or with cement treatment. Lowland Technology International 3:1-13.

52. Yin JH (2004) Properties and behavior of a cement mixed Hong Kong marine clay and design applications. In: Proceedings of Ground Treatment, Hong Kong Geotechnical Society, Hong Kong, pp 97–105.

53. Yin JH, Fang Z (2006) Physical modelling of consolidation behaviour of a composite foundation consisting of a cement-mixed soil column and untreated soft marine clay. Geotechnique 56(1):63-68. https://doi.org/10.1680/geot.2006.56.1.63

54. Yin JH, Fang Z (2010) Physical modeling of a footing on soft soil ground with deep cement mixed soil columns under vertical loading. Marine Georesources and Geotechnology 28(2):173-188. https://doi.org/10.1080/10641191003780872

55. Yin JH, Graham J, Clark JI, Gao L (1994) Modelling unanticipated pore-water pressures in soft clays. Canadian Geotechnical Journal 31(5):773-778. https://doi.org/10.1139/t94-088

56. Yu X, Zheng G, Zhou H, Chai J (2021) Influence of geosynthetic reinforcement on the progressive failure of rigid columns under an embankment load. Acta Geotechnica 16(9):3005-3012. https://doi.org/10.1007/s11440-021-01160-6

57. Zaeske D (2001) Zur Wirkungsweise von unbewehrten und bewehrten mineralischen Tragschichten über pfahlartigen Gründungselementen. Fachgebiet u. Versuchsanst. Geotechnik, Univ. Gh Kassel.

58. Zhang J, Zheng JJ, Chen BG, Yin JH (2013) Coupled mechanical and hydraulic modeling of a geosynthetic-reinforced and pile-supported embankment. Computers and Geotechnics 52:28-37. https://doi.org/10.1016/j.compgeo.2013.03.003

59. Zheng G, Yang X, Zhou H, Chai J (2019) Numerical modeling of progressive failure of rigid piles under embankment load. Canadian Geotechnical Journal 56(1):23-34. https://doi.org/10.1139/cgj-2017-0613

858 **Tables and Figures**
859

860 Table 1. Basic properties of Hong Kong marine deposits (HKMD) and sand

HKMD	G_s	Atterberg limits LL (%)	PL (%)	PI (%)	w_0 (%)	pH	Loss of ignition (%)	φ' (◦)	C_e/V	C_c/V	$C_{\alpha e}/V$
	2.65	43.2	22.6	20.6	100	6.44	4.46	24	0.03	0.24	0.002

Sand	G_s	ρ_d (Mg/m^3) max	min	w_{opt} (%)	d_{10} (mm)	d_{30} (mm)	d_{60} (mm)	φ' (◦)
	2.56	1.742	1.536	16.5	0.17	0.27	0.59	34.6

861 Note: G_s is the specific gravity, LL is the liquid limit, PL is the plastic limit, PI is the
862 plasticity index, w_0 is the initial water content, C_e/V is the slope of unloading/reloading line,
863 C_c/V is the slope of normal consolidation line of the reconstituted HKMD, $C_{\alpha e}/V$ is the creep
864 coefficient, ρ_d is the dry density, w_{opt} is the optimum water content.
865
866
867
868 Table 2. Scaling of variables

Parameter	Scaling	Dimension
Time	1	[T]
Stress	1	[M/LT^{-2}]
Length	1:x	[L]
Stiffness of geotextile	1:x	[MT^{-2}]
Tensile strength of geotextile	1:x	[MT^{-2}]
Area	1:x^2	[L^2]
Force	1:x^2	[MLT^{-2}]
Strength of soil and columns	1	[M/LT^{-2}]

869
870
871

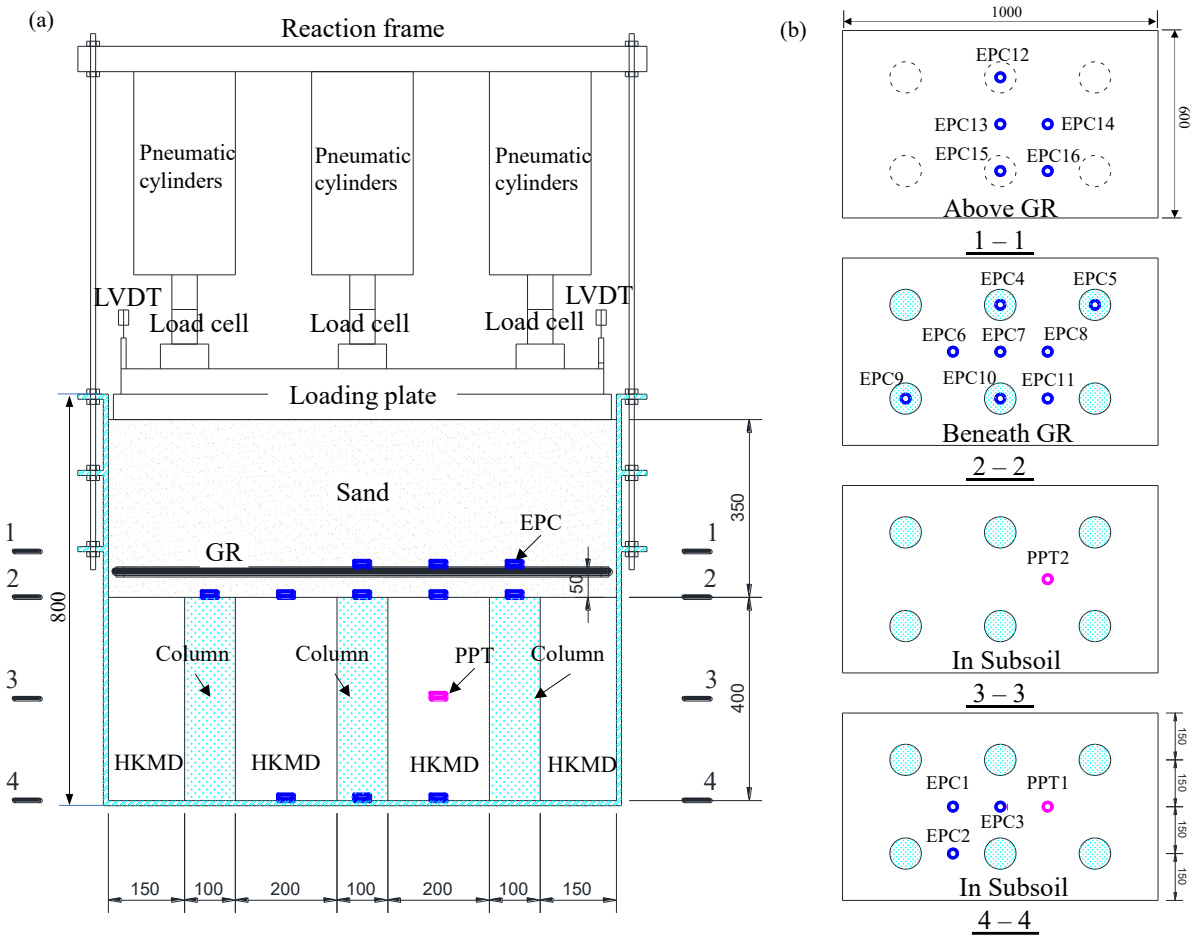

872

873 Figure 1. Test setup and the layout of transducers (unit in mm) – (a) longitudinal cross-
874 section and (b) four horizontal cross-sections

875

876

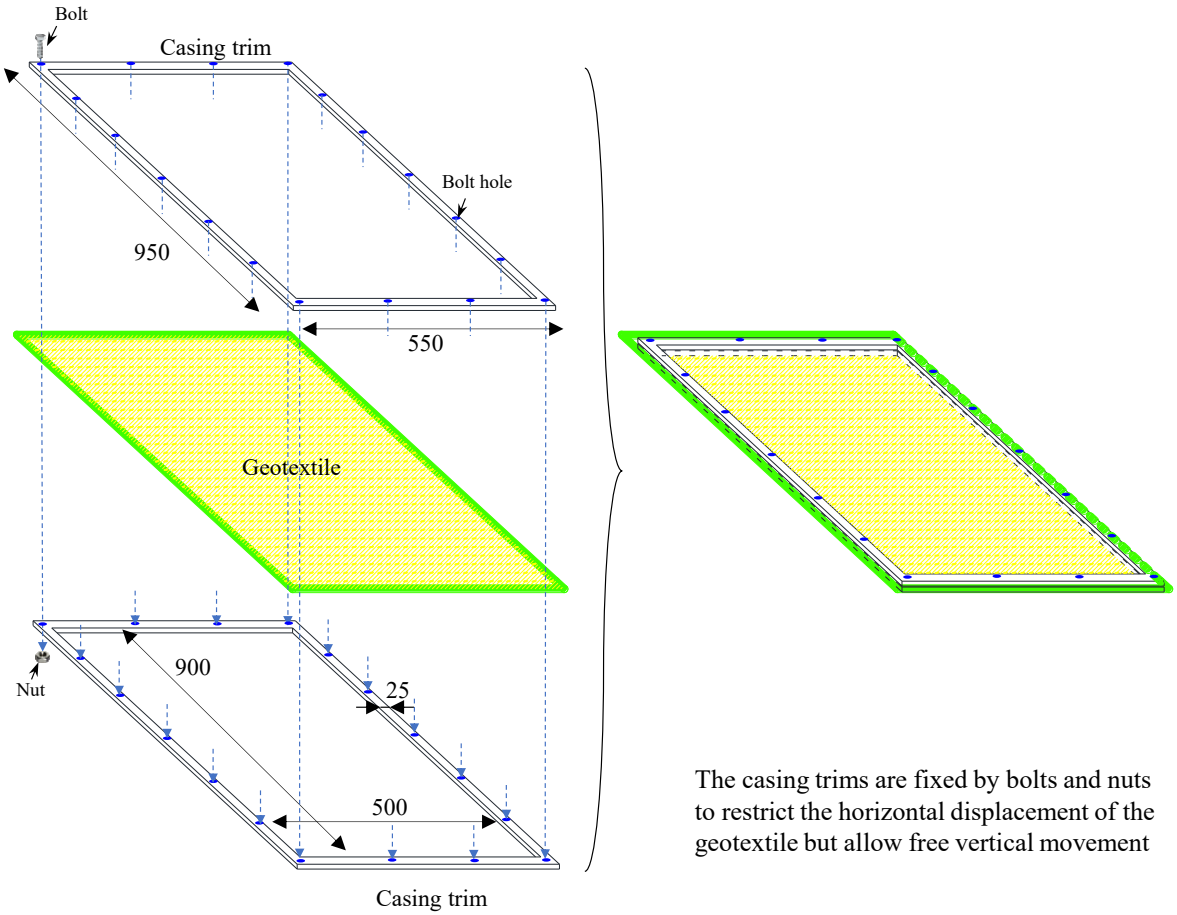

877

878 Figure 2. Illustration of casing trims for fixing geotextile (unit in mm)

879

880

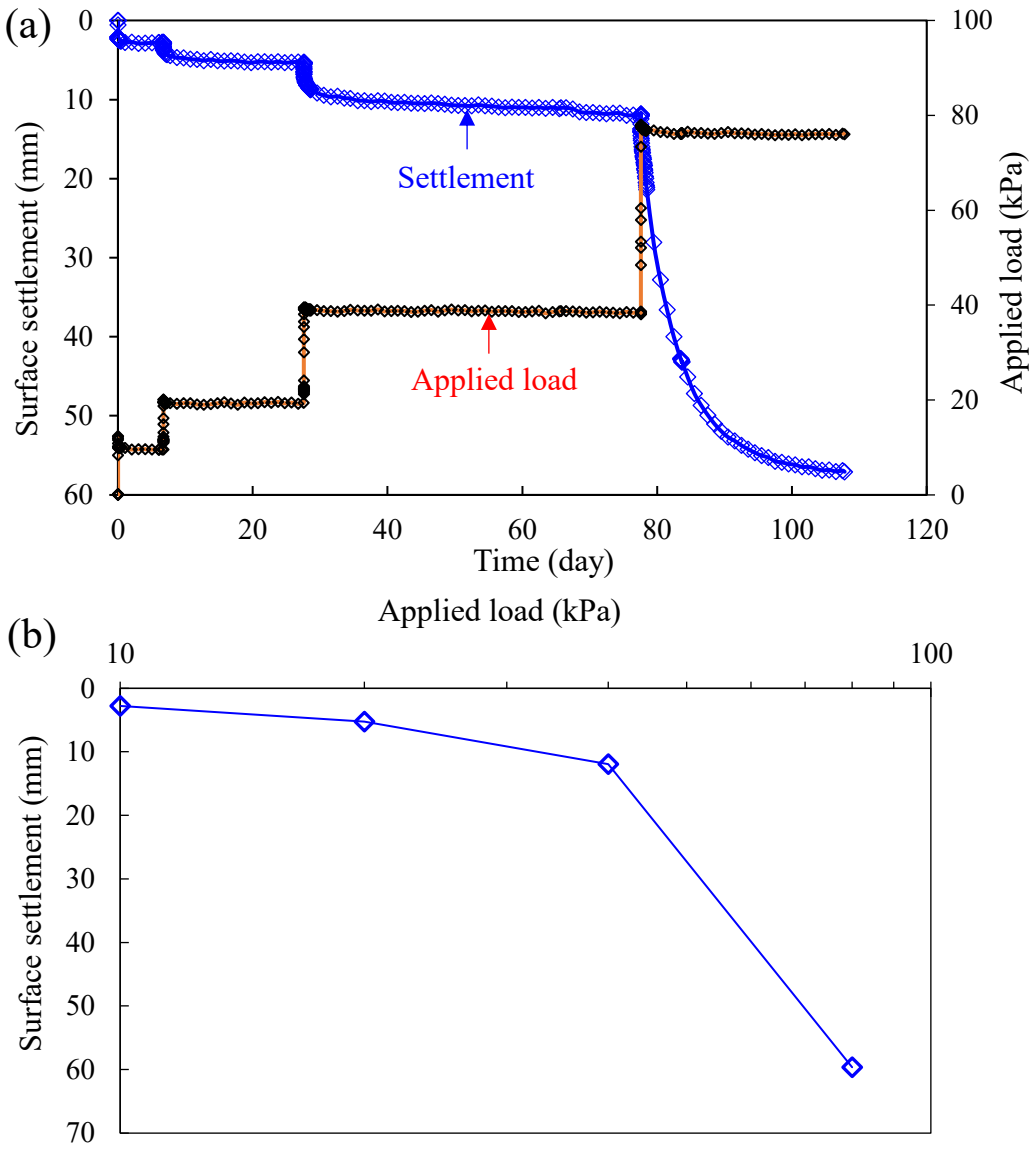

881

882 Figure 3. (a) Measured surface settlement and applied load with time and (b) Surface
883 settlement versus applied load (log scale)

884

885

886

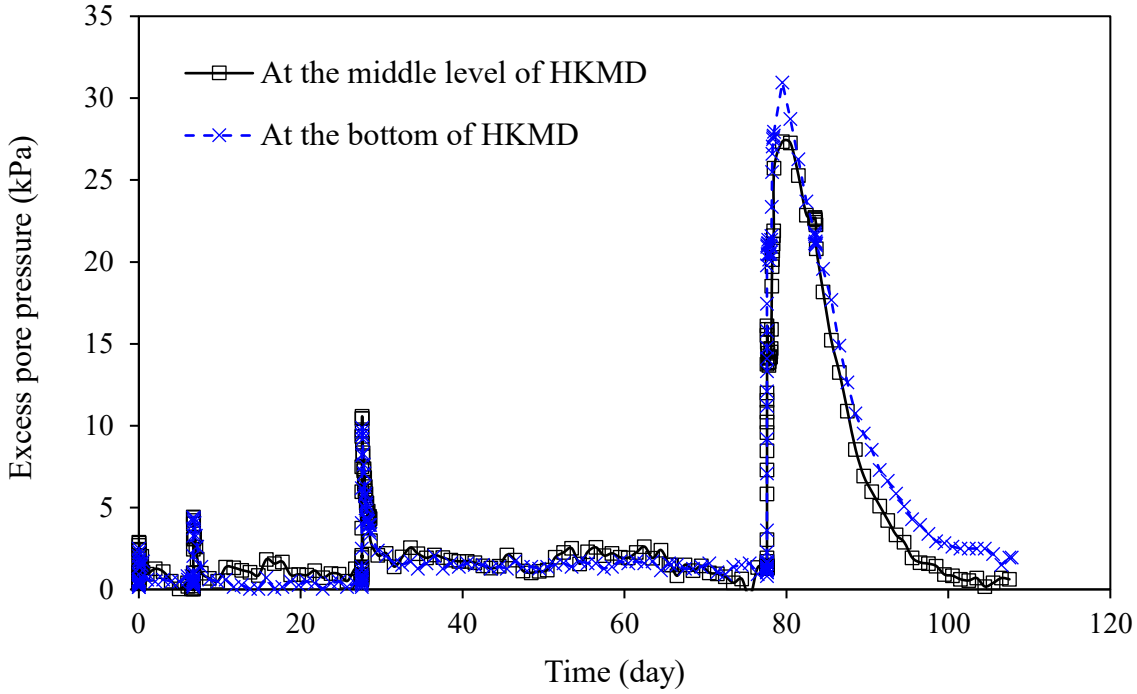

887

888 Figure 4. Measured excess pore pressures with time at different locations in HKMD

889

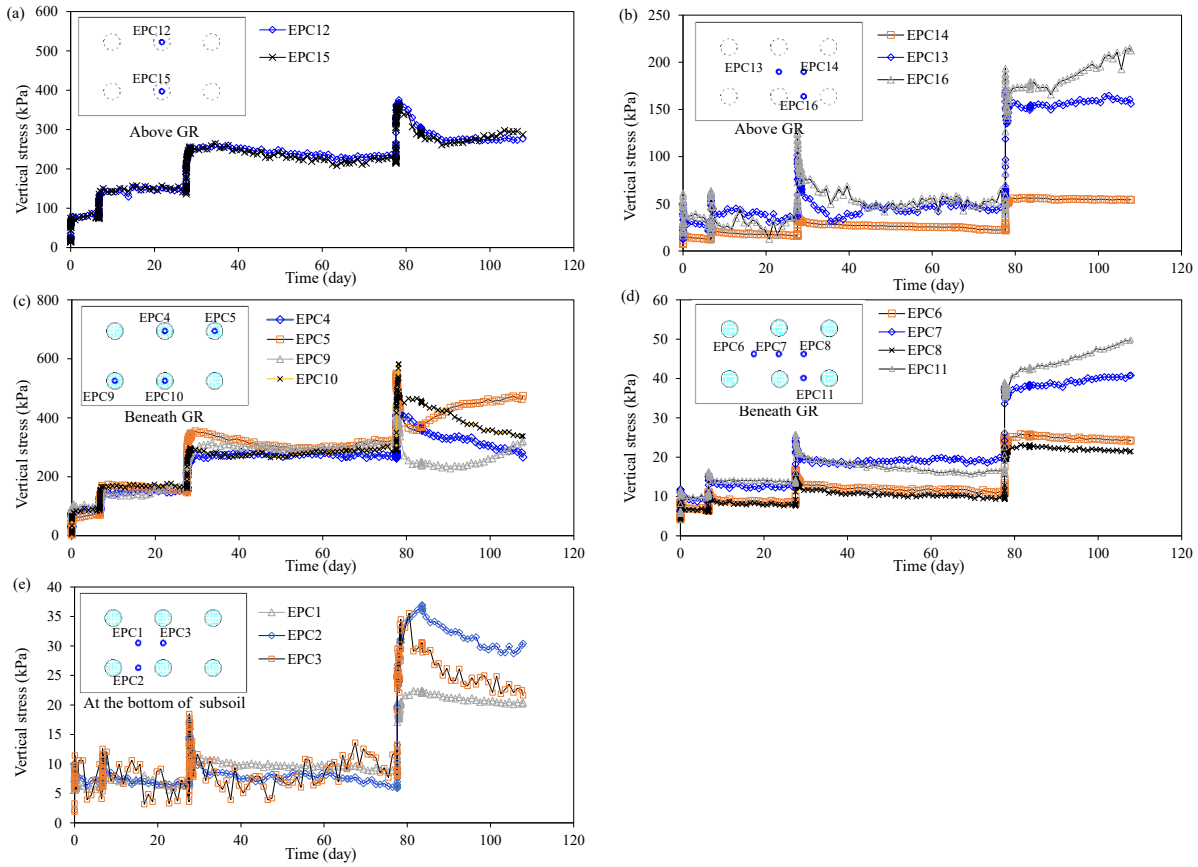

890

891 Figure 5. Measured vertical stresses at the locations of (a) EPCs 12, 15; (b) EPCs 13, 14, and
892 16; (c) EPCs 4, 5, 9, and 10; (d) EPCs 6, 7, 8, and 11; and (e) EPCs 1~3

893

894

895

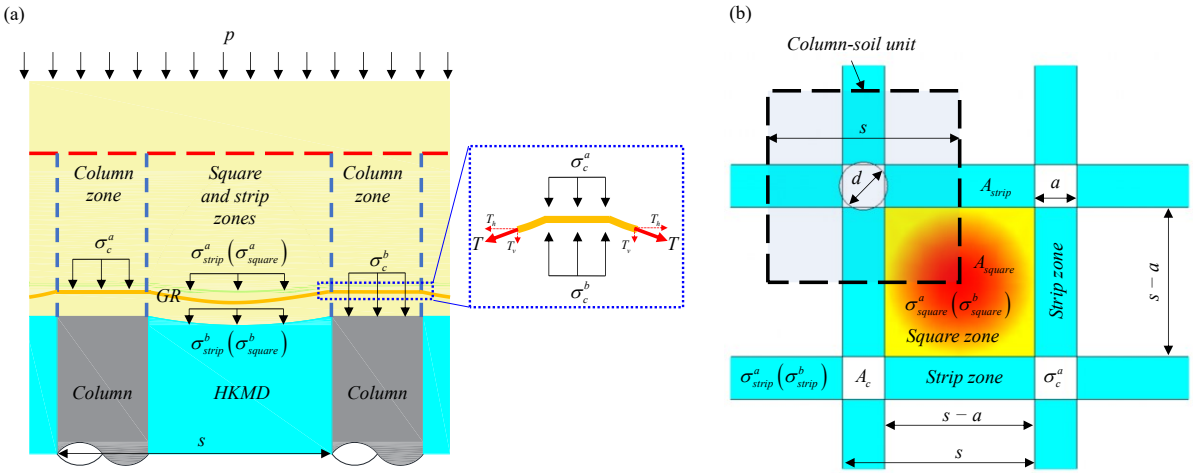

Figure 6. Illustration of (a) column, square, and strip zones and (b) column-soil unit

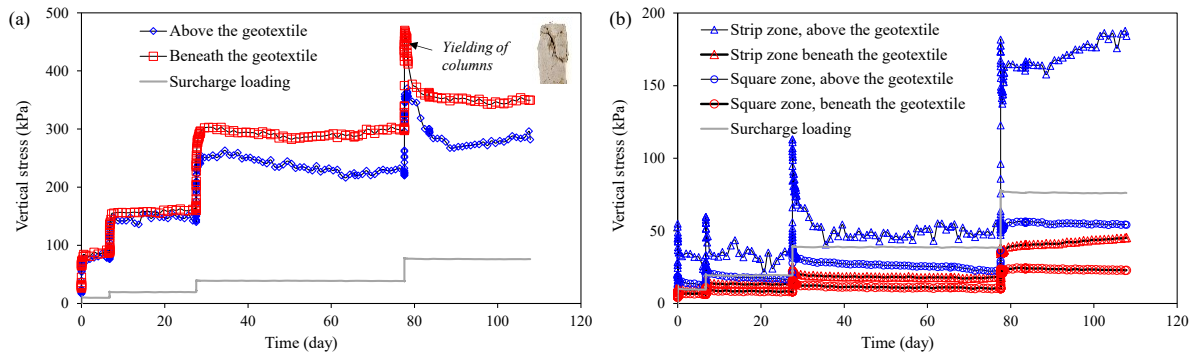

899

900 Figure 7. Vertical stresses above and beneath the geotextile in (a) column zones and (b) strip
901 and square zones

902

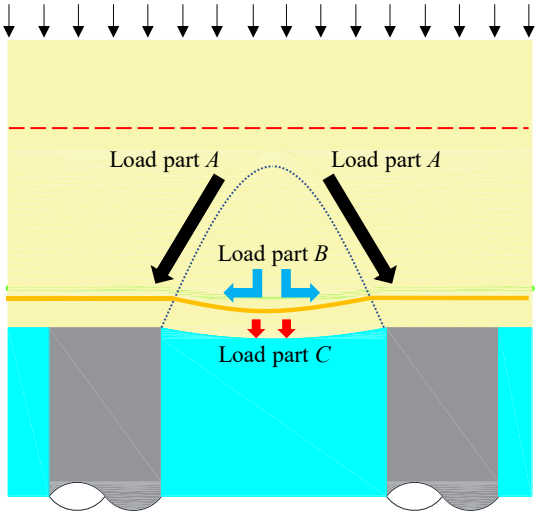

Figure 8. Illustration of load parts *A*, *B*, and *C*

911

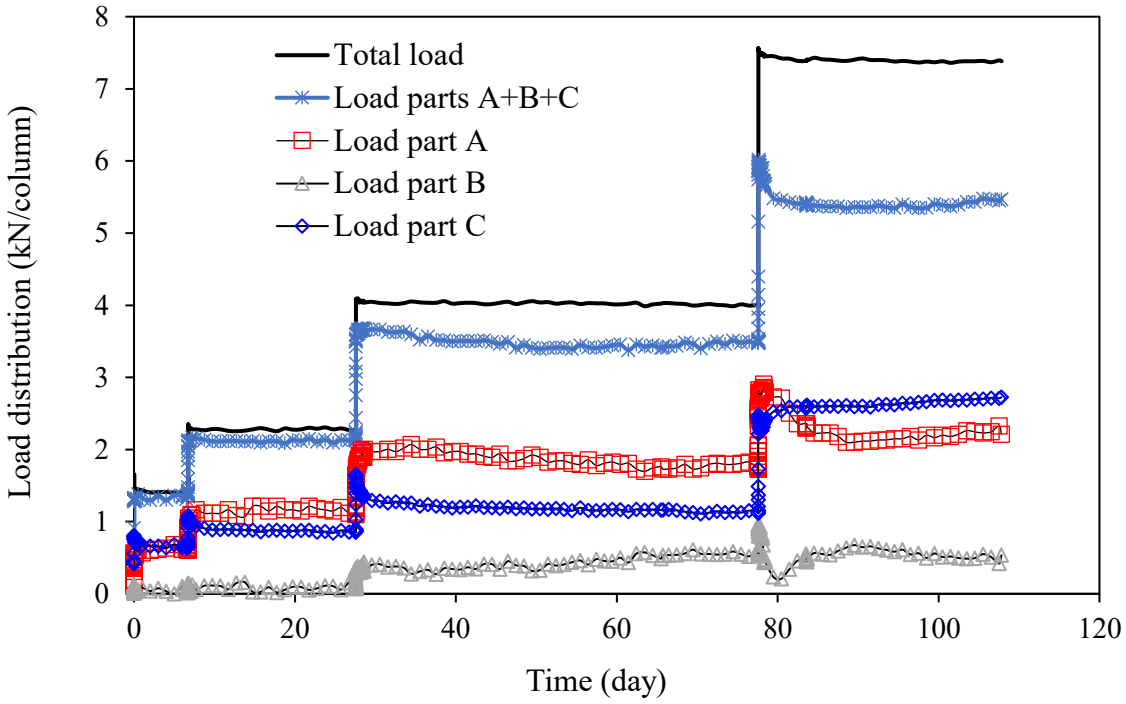

912

913 Figure 9. Load distribution in a column-soil unit regarding load parts *A*, *B*, and *C*

914

915

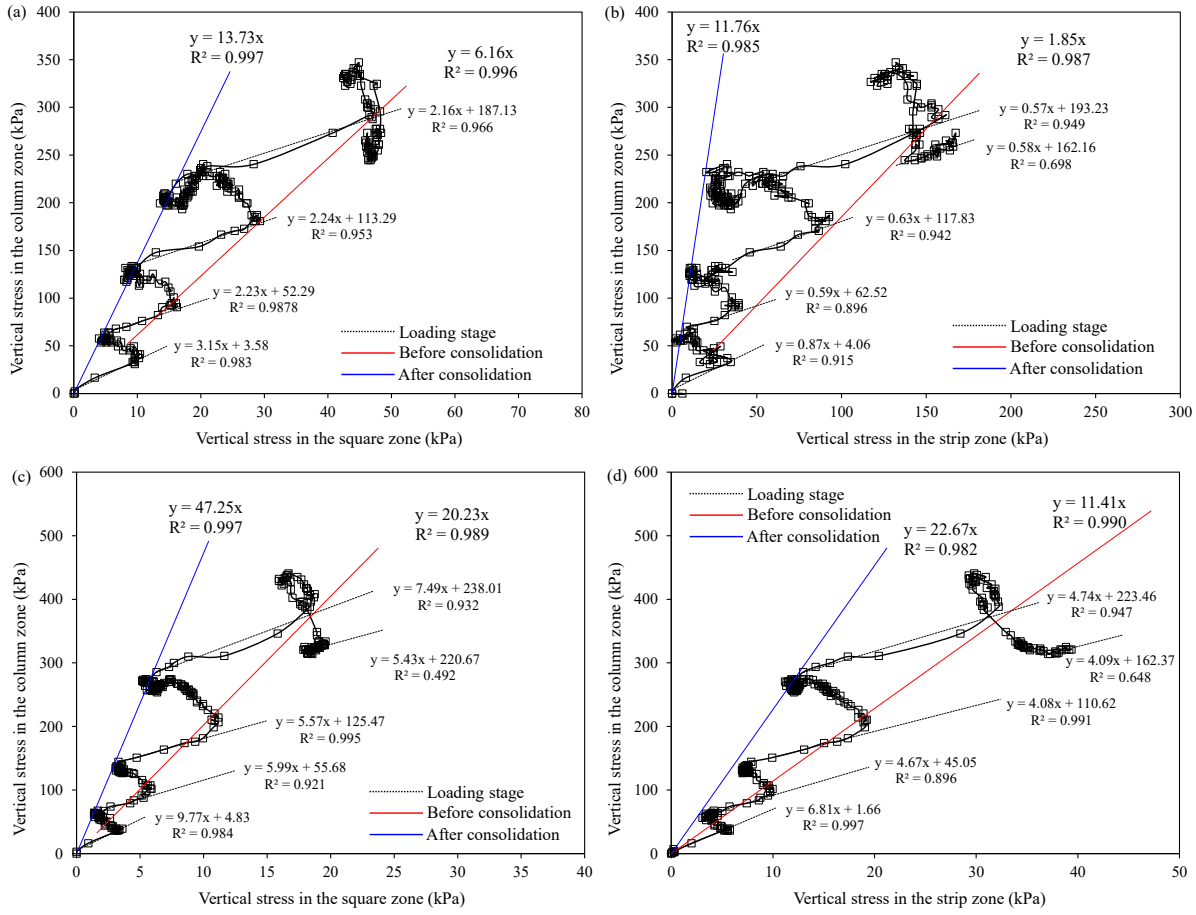

916

917 Figure 10. Relationship between vertical stresses in (a) column zone versus square zone
918 (above the geotextile), (b) column zone versus strip zone (above the geotextile), (c) column
919 zone versus square zone (beneath the geotextile), and (d) column zone versus strip zone
920 (beneath the geotextile)

921

922

923

924

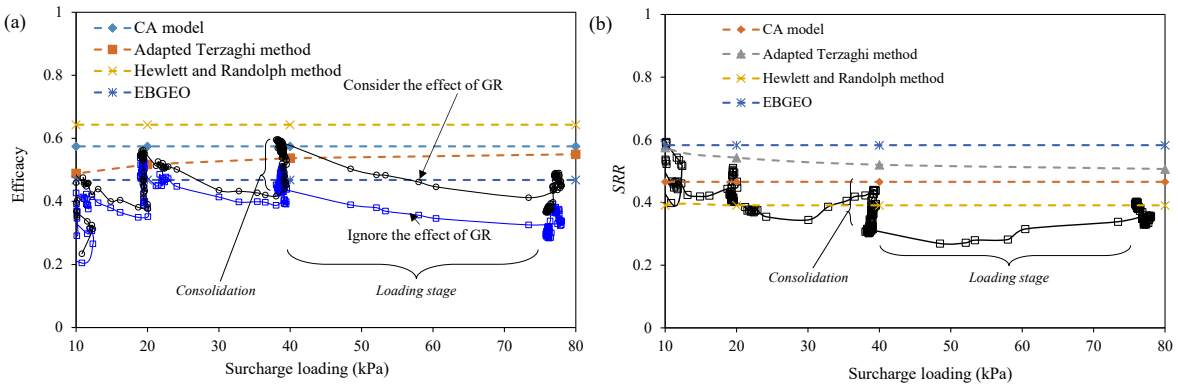

925 Figure 11. (a) Efficacies and (b) stress reduction ratios calculated by measured data and
926 estimated by different methods under different surcharge loads

927

928

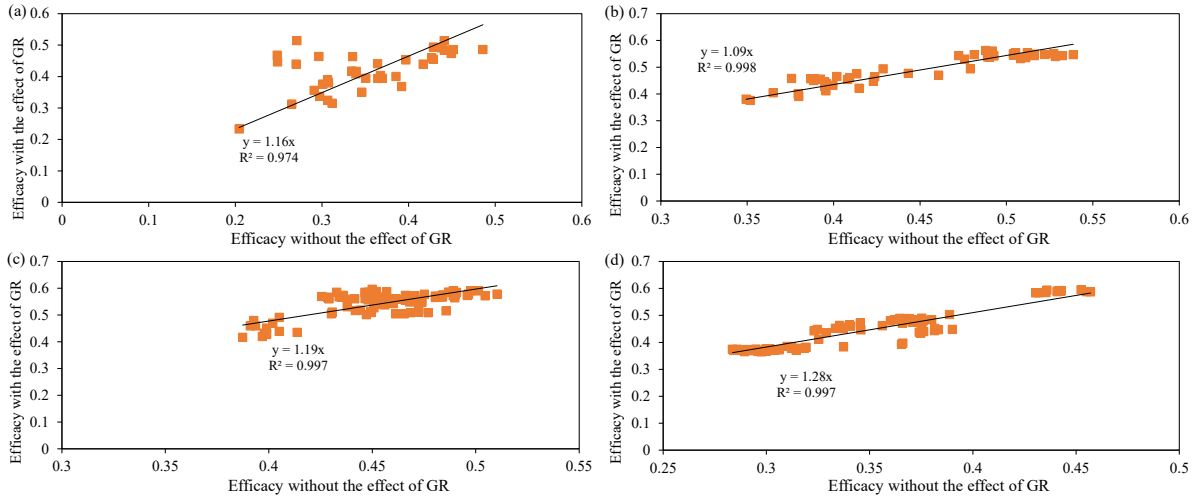

929 Figure 12. Relationship between efficacies with and without the effect of GR under the
930 surcharge loads of (a) 10 kPa, (b) 20 kPa, (c) 40 kPa, and (d) 80